# Simultaneous Shack-Hartmann and digital holography measurements of the optical effect of a subsonic compressible shear layer

Carson M. Kipp*[a], Timothy J. Bukowski[a], R. Mark Rennie[a], and Stanislav Gordeyev[a]

[a]Institute of Flow Physics and Control, Aerospace and Mechanical Engineering Department, University of Notre Dame, Notre Dame, IN, USA

## ABSTRACT

The compressible shear layer is an important fundamental flow for the determination of aero-optical effects on airborne beam directors. Past research has shown disagreement in regards to the magnitude of thermodynamic gradients between the predictions of computational fluid dynamics (CFD) simulations and experimental data for the aero-optical effect of the shear layer. One reason these density-related discontinuities were not observed experimentally is that Shack Hartmann wavefront sensors (SHWFS), used to study shear layers optically, cannot resolve the sharp wavefront gradients in the flow using standard algorithms. One way to resolve this issue is to employ a digital holographic (DH) measurement approach which directly measures the phase of the optical aberration. In this paper, a comparison is presented of simultaneous SHWFS and DH measurements of the optical wavefront on a laser beam propagating in the cross-stream direction through a subsonic shear layer. In addition to processed wavefronts, a comparison of the analysis methods employed, as well as pros and cons for each technique is presented. The findings have general application to the measurement of optical wavefronts containing steep OPD gradients.

**Keywords:** Aero-optics, digital holography, Shack-Hartmann wavefront sensing, shear layer, thermodynamic gradients

## 1. INTRODUCTION

### 1.1 Aero-Optics Fundamentals

Aero-optics is the study of the optical effects caused by index of refraction gradients induced by compressible flows. The index of refraction, defined as the ratio of the speed of light in a vacuum to the speed of light in a particular medium, is a function of the medium's density.[1,2] Although electromagnetic (EM) waves are affected by density gradients in all types of flows, aero-optic studies focus on that of compressible flows due to the intense and highly variable density fields. In air, the index of refraction, $n$ is defined as a function of air density, $\rho$ , in the Gladstone-Dale equation:

$$n = 1 + K_{GD}\rho, \tag{1}$$

where $K_{GD}$ is the Gladstone-Dale coefficient. The Gladstone-Dale equation implies that any flow field exhibiting large density gradients will exhibit corresponding index of refraction gradients. The Gladstone-Dale coefficient is a weak function of wavelength and is defined by Barrell and Sears[3,4] as

$$K_{GD} = 2.223 \times 10^{-4} \left\{1 + 5.669 \times 10^{-3}/\lambda[\mu\text{m}]^2\right\} \ [\text{m}^3\text{kg}^{-1}] \tag{2}$$

The effect of aero-optical aberrations on system performance is clearly demonstrated by Gordeyev et. al in Ref. 4 in their examination of diffraction limited intensity in the context of Strehl ratio. Here the maximum intensity is defined as the highest physically possible intensity of an EM wave on a target, achieved in the absence of optical aberrations along the propagation path of the wave (so-called diffraction limited intensity). Gordeyev et. al illustrate how maximum or diffraction limited intensities vary with wavelength by showing normalized values for several common lasers in Fig. 1 on the left.

*Corresponding Author. E-mail: ckipp@nd.edu, Telephone: (248) 766-2860

Unconventional Imaging, Sensing, and Adaptive Optics 2025, edited by Jean Dolne, Santasri Bose-Pillai, Matthew Kalensky, Proc. of SPIE Vol. 13619, 136190P · 2025 Published by SPIE
0277-786X · doi: 10.1117/12.3063229

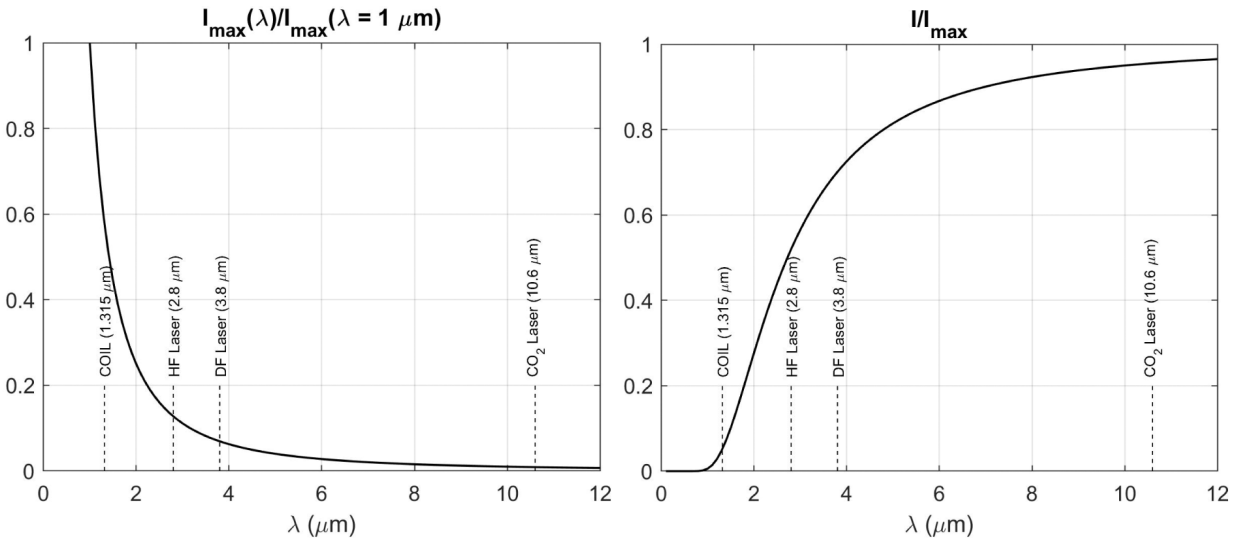


Figure 1. Maximum diffraction limited intensity normalized by an EM wave of wavelength 1 $\mu m$.(left) Strehl ratio as a function of wavelength undergoing optical aberrations which degrade the intensity on target by 5% for a 10.6 $\mu m$ laser. (right) Both adapted from Ref. 4.

As indicated by the figure, intensity on target depends on the wavelength, $\lambda$, as $I \sim 1/\lambda^2$ and defines the operational capabilities of EM systems in the absence of aberrations. While a shorter wavelength wave offers greater theoretical intensity on target, aero-optical distortions imposed on the EM beam will reduce the resulting beam intensity on a target. A useful parameter for describing this phenomenon is the Strehl Ratio, $SR$, which is defined as the ratio of the instantaneous intensity on target for an EM wave to that of its respective maximum (diffraction limited) intensity, $SR = I/I_{max}$. In effect, it is a measure of the performance of an optical system in the presence of aberrations. Under some simplifying assumptions, the Large-Aperture Approximation can be used to calculate the Strehl Ratio as (Ref. 4)

$$SR \approx exp\left(\left[-\frac{2\pi}{\lambda} OPD_{rms}\right]^2\right) \tag{3}$$

From here it follows that for the same level of aero-optical distortions, defined as $OPD_{rms}$, the Strehl Ratio decreases with decreasing wavelength, as shown in Fig. 1 on the right.

Thus, while shorter wavelengths provide higher theoretical intensity on the target, their propensity for greater optical aberrations often reduces their practical performance in aero-optic environments. The lower-wavelength limit, set by optical aberrations, can be extended through active adaptive optics or passive aerodynamic flow control if the flow field is well understood. This motivates aero-optical study.

## 1.2 Background and Motivation

One of the most common types of aberrating flows optical systems may encounter is the compressible shear layer. This scenario often arises when hemispherical turrets are used as the beam director on airborne systems, a common choice due to their simplified geometry and wide field of regard.[4,5] However, this geometry tends to induce regions of separated flow, which in turn forms a compressible shear layer through which an EM wave must propagate if it is oriented in the downstream direction. The compressible shear layer gives rise to strong optical aberrations which are associated with the reduced pressure and density inside discrete shear-layer vortices, and which limit the intensity on target for an EM wave propagating through the shear layer.

Wells et. al. in Ref. 6 sought to quantify the magnitude of the gradient of thermodynamic properties in compressible shear layers. However, their study found evidence that the commonly used Shack-Hartmann wavefront sensor (SHWFS) is inadequate for resolving sharp thermodynamic gradients present in compressible

shear layers and other heavily aberrating flows, as the reconstruction algorithms tend to force the wavefronts to be continuous and are unable to resolve near-discontinuous density gradients.[7,8] The SHWFS uses a lenslet array to focus the beam onto a CCD array creating a grid of dots, after which the resulting images are analyzed to infer properties of the underlying density field. An example of the dot pattern of a SHWFS measurement can be seen below in Fig. 2. Specifically, the group found that measurement of the compressible shear layer resulted in

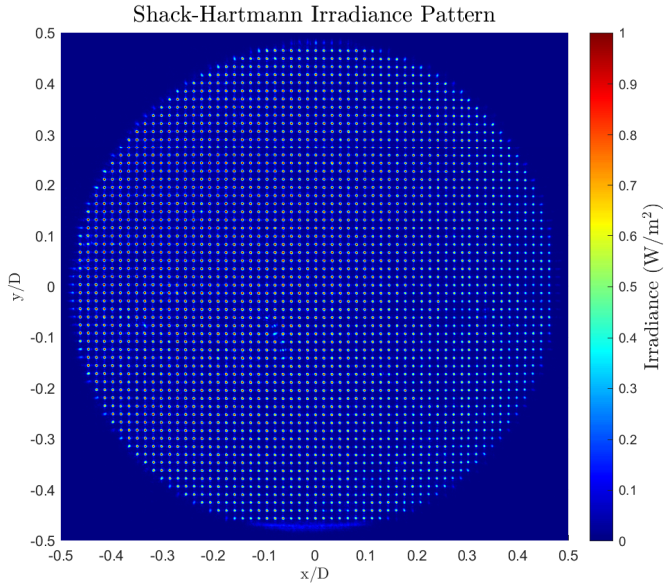


Figure 2. Shack-Hartmann lenslet array irradiance plot

appreciable beam spreading (an indicator of data degradation) of the focused dots from lenslets along the shear-layer slip line location. This beam spreading is the result of diffraction of the beam at individual lenslets due to a strong index-of-refraction gradient at the beam location corresponding to the lenslet. The inaccuracy of the SHWFS measurements were further implied by disagreement between the experimental data and complementary computational fluid dynamics (CFD) results. To quantify the beam-spreading effect for individual lenslets, the second-moment beam width, or D4$\sigma$, was used. The equation for D4$\sigma$ in the x direction is given in Equation (4) below:

$$D4\sigma_x = 4\sqrt{\frac{\int_{-\infty}^{\infty}\int_{-\infty}^{\infty} I(x,y)(x-\bar{x})^2\,dx\,dy}{\int_{-\infty}^{\infty}\int_{-\infty}^{\infty} I(x,y)\,dx\,dy}} \tag{4}$$

where $I(x,y)$ is the beam intensity profile and $\bar{x}$ is the beam centroid. D4$\sigma$ is a measure of deviation of the irradiance distribution within a lenslet from the centroid location of the beam, indicating a beam that has likely been spread out due to diffraction effects, and hence likely degradation of data. Appreciable D4$\sigma$ values can arise from a number of sources including higher order aberrations (aberrations of a smaller spatial scale than that of the given lenslet), nonuniform illumination and phase discontinuities. For the purpose of this paper, it was assumed that beam spread due to nonuniform illumination and was negligible. That is, the spreading of the beam is assumed to be primarily due to higher order aberration and high-magnitude phase gradients.[7,9,10]

This paper describes an experimental effort to measure and compare the wavefronts, associated with the density gradients in the shear layer, using Shack-Hartmann and digital-holographic wavefront sensors. In particular, digital holographic measurements were employed to address the issue of spatial resolution and improved performance in resolving sharp phase gradients, allowing us to resolve both higher order aberrations and high-magnitude thermodynamic gradients. In future work, the performance of the two methods will also be compared

with complementary CFD data in order to better understand the existence and magnitude of sharp thermodynamic gradients within compressible shear layers.

## 2. EXPERIMENT

### 2.1 Wind Tunnel and Test Section

To compare the performance of the two techniques, simultaneous digital holographic and Shack-Hartmann wavefront measurements were performed in the Compressible Shear Layer Wind Tunnel (CSLWT) at the University of Notre Dame (UND). The tunnel forms a shear layer at transonic speeds by utilizing two inlets of differing speeds which draw from a common reservoir. The high-speed inlet produces a freestream Mach number of $M_2 \approx 0.71$ ($U_2 \approx 231$ m/s) while the low-speed inlet produces a freestream Mach number of $M_1 \approx 0.17$ ($U_1 \approx 57$ m/s). The low-speed inlet features a "straw box" section which serves to reduce the total pressure of the incoming air such that the static pressure is uniform in the wind-tunnel test section, whereas the high-speed inlet features a shorter "straw box" which serves to improve flow quality.[6] In addition, because both inlets draw from the same laboratory environment, total temperatures match for the inlets. The two inlets merge in the test section via a splitter plate with a width of approximately 0.1143 m (4.5 inches). The convective mach number for the test conditions was $M_c \approx 0.26$ as calculated using Equations (5) and (6) where subscripts 1 and 2 denote high and low speed flow respectively.[11]

$$M_C = \frac{(U_1 - U_C)}{a_1} \tag{5}$$

$$U_C = \frac{(a_2 U_1 + a_1 U_2)}{a_1 + a_2} \tag{6}$$

Three speakers were embedded in the trailing edge of the splitter plate and were synchronized and excited at a frequency close to the natural convective frequency of vortical structures within the flow at the location of the measurement beam. Previous studies[12] showed that this flow forcing regularizes the shear layer downstream of the splitter plate increasing spanwise uniformity of the flow. This allows the optical measurements to better resolve the thermodynamic structure of individual shear-layer vortices, which will later be compared to two-dimensional CFD simulations that are currently being run as part of this research effort.

### 2.2 Optical Table

A schematic of the double-pass optical setup used to take measurements of the flow is shown in Fig. 3, and a photograph of the populated optical table is shown in Fig. 4. A 532 nm yttrium aluminum garnet (YAG) solid state continuous laser was passed through a collimator, expanding the beam to 25.4 mm (1 inch). This expanded beam was then split into its reference and signal components to be used in digital holography using a 50/50 beam splitter cube. The signal beam was then traversed upwards to the height of our test section using a periscope, passed through a 4f reimaging telescope (for the return leg), and then expanded to 0.1016 m (4 inch) which was passed through the wind tunnel test section. Note that the beam was passed through the shear layer in the cross-stream direction, in order to capture the optical distortion of the shear-layer vortices in profile, to better understand the origin of aero-optical aberrations within the vortices. Measurements were taken approximately 0.279 m (11 inches) downstream of the splitter plate. The beam was then reflected from a large return mirror and sent back through the test section creating a double-pass configuration. The signal beam then returns along the same optical path, deviating when it reaches the 50/50 beam splitter cube located just after the periscope on its return. This beam splitter cube redirected the signal beam into the simultaneous digital holography and Shack-Hartmann measurement apparatus, where the signal beam was further split into the components to be measured by digital holographic and Shack-Hartmann sensors and passed through another reimaging telescope. The surface of the return mirror was chosen as the image location to reduce beam wander on the sensors due to vibration. After this final split the Shack-Hartmann portion of the beam was directed through a lenslet array into a Phantom v1611 high-speed camera. The lenslets in the array had a pitch of 0.3 mm and a focal length of 38 mm, providing a wavefront resolution of 60 by 59 pixels. The digital holographic signal beam was recombined

with the tilted reference and the resulting hologram was captured on a Phantom v2512 high-speed camera. The measured digital holographic wavefront had a resolution of 161 by 161 pixels. To collect simultaneous data for both wavefront sensing techniques, the two high-speed cameras were connected in series to a function generator. To initiate data collection, a transistor-transistor logic (TTL) pulse from the function generator was sent to both cameras ensuring simultaneous data collection within $1/f_s$ seconds, where $f_s$ is the frame rate of the camera. Optical measurements were taken at 20000 Hz.

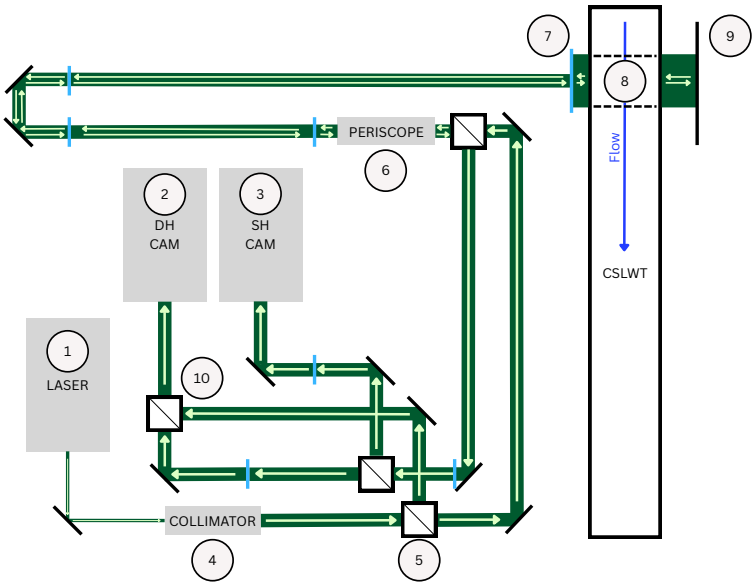


Figure 3. Diagram of experimental optical setup with lenses colored light blue and mirrors black 1) 532 nm YAG laser 2) high-speed camera used for digital holographic measurements 3) high-speed camera used for Shack-Hartmann wavefront sensing 4) 1 inch beam collimator 5) 50/50 beam splitter cube 6) periscope 7) 4 inch lens 8) test section 9) 10 inch mirror corresponding to image plane 10) Recombination location of signal and reference digital holography beams

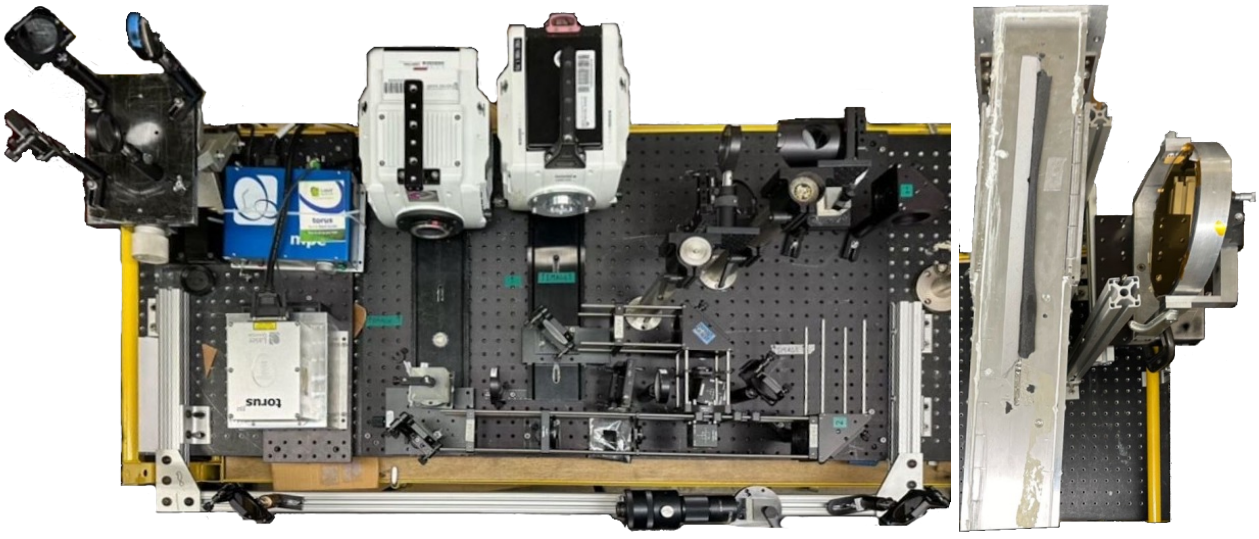

Figure 4. Experimental optical table layout

### 2.3 Shack-Hartmann Wavefront Sensing

Shack-Hartmann wavefront sensing measures the OPD field by analyzing the displacement of the dots formed by the lenslet array. The OPD is defined as the deviation from the spatially averaged optical path length (OPL), and is also equal to the negative of the wavefront. The optical path length represents the distance light travels in a vacuum in the same time it travels some distance in a medium and is given by:[4]

$$OPL(x,y,t) = \int n(x,y,z,t)\,dz = \int \left[1 + K_{GD}\rho(x,y,z,t)\right]\,dz \tag{7}$$

Correspondingly, the optical path difference is:

$$OPD(x,y,t) = OPL(x,y,t) - \langle OPL(x,y,t)\rangle = K_{GD}\int_A^B \rho'(x,y,z,t)\,ds, \tag{8}$$

Each dot formed by the lenslet array will experience differing optical aberrations due to density variations in the flow field. As such, the OPD quantifies deviations from the mean optical aberration across the array. To determine OPD, the method employs trigonometric relations involving the focal length of the lenslets, $f$, and the displacement in each spatial direction, $\Delta x_k$ and $\Delta y_k$, which in turn can be related to wavefront via Equations (9) and (10) as described by Ref. 4.

$$\left(\frac{\partial w}{\partial x}\right)_k \approx -(\theta_x)_k = -\frac{\Delta x_k}{f}, \tag{9}$$

$$\left(\frac{\partial w}{\partial y}\right)_k \approx -(\theta_y)_k = -\frac{\Delta y_k}{f}, \tag{10}$$

where $((\frac{\partial w}{\partial x})_k,\ (\frac{\partial w}{\partial y})_k)$ is the two dimensional wavefront slope of a given sub-region. It is important to note that the displacements $\Delta x_k$ and $\Delta y_k$ are measured relative to the dot locations without flow-induced aberrations in order to remove the effects of steady aberrations resulting from the optical system. A representative comparison of the lenslet array with and without flow is shown in Fig. 5.[13]

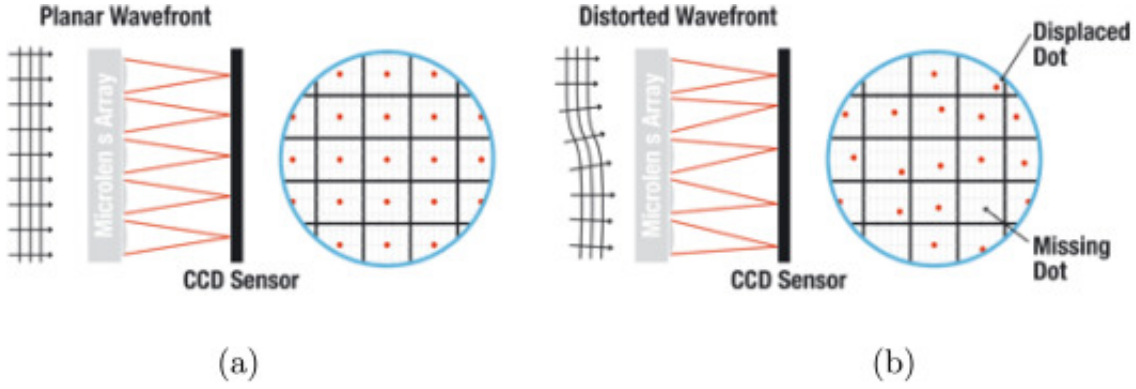


Figure 5. Shack-Hartmann lenslet arrays for the a) no flow induced case b) flow induced case from Ref. 13

To reconstruct the wavefront from the measured slopes, the Southwell method was applied using a least squares surface reconstruction approach.[14] Finally, the tip, tilt, and piston components of the reconstructed wavefront were removed, where piston describes the constant offset of the wavefront, and tip and tilt correspond to the linear slope of the full wavefront along the x and y axes, respectively. One limitation of Shack-Hartmann wavefront sensing is that the resolution of this reconstructed wavefront corresponds to the number of lenslets in the array, which is notably less than methods such as digital holography.

## 2.4 Off-Axis Digital Holography

The other optical measurement technique employed within this study was off-axis digital holography. Digital holography measures both amplitude and phase and provides much higher resolution than Shack-Hartmann.[15–17] Off-axis digital holography uses the wavelike nature of light in order to measure wavefronts and subsequently infer density fields. It works by overlapping a signal beam from a laser with long coherence length, which passes through the flow of interest, with a tilted reference beam that is passed directly from the laser onto the camera.

At its core, digital holography is an interferometric technique. It draws conclusions about the aberrated wavefront by analyzing the spatial frequency content of the interference pattern formed between the signal and reference beams.[18] In our setup we used the off-axis pupil plane recording geometry, where the collimated laser beam was interfered with a tilted collimated reference laser beam. This implementation of digital holography has been studied thoroughly in the literature.[16,19–21] The tilt angle determines the spatial frequency of the resulting interference fringes: the larger the angle, the higher the fringe frequency.

The relationship between beam angle and fringe pattern spatial frequency can be visualized by considering the signal beam as a collection of photons treated as waves. When the signal beam is angled relative to the reference beam, the signal beam's waves must travel slightly farther to reach the same point on the camera sensor. This difference in path length causes adjacent waves to arrive increasingly out of phase, as illustrated in Fig. 6.

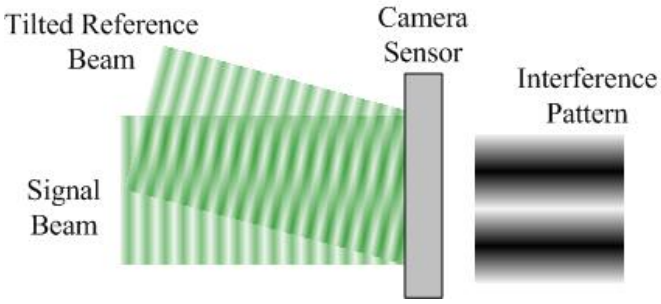


Figure 6. Incident beam phase diagram, demonstrating how the angle between signal and reference beams affects the spatial frequency of the resulting fringe pattern

As shown in Fig. 6, adjacent waves arrive increasingly out of phase, and as this incident angle is increased, the phase differential between adjacent waves grows larger. The interference of the signal and reference beams forms a fringe pattern, where the spatial frequency of the fringes is directly related to the incident angle of the signal beam as seen in Fig. 7 from Ref. 18. Understanding this relationship is crucial, as it later allows us to "shift" the wavefront information in the 2-D Fourier domain, thereby separating it from noise and other artifacts.

When the wind-tunnel flow is turned on, aero-optical aberrations from the flow introduce spatial variations in the fringe pattern. These variations arise from changes in the local phase, which alter the spatial frequency of the fringes across the pattern. By applying the fast Fourier transform (FFT) to the resulting interferogram, the fringe pattern can be decomposed into its spatial frequency components. The region in the 2-D Fourier domain corresponding to the optical aberrations induced by the flow can then be isolated, as shown by the red circle in Fig. 8.

Once isolated, the inverse fast Fourier transform (iFFT) of this region can be used to reconstruct the complex optical field (COF) which contains both amplitude and phase information about the measured interferogram. As with Shack-Hartmann wavefront sensing, the COF resulting from the optical setup was captured with the wind tunnel off and this aberration removed from the following flow-on cases by dividing the COF by the no flow case. The initially wrapped modulo-$2\pi$ phase component of the COF was then unwrapped using a least squares unwrapping algorithm and converted to a wavefront by multiplying by $\frac{\lambda}{2\pi}$ . Tip, tilt, and piston were also subtracted from the COF.

Importantly, the resolution of digital holography is limited primarily by the camera resolution and size of the area selected in the Fourier domain as in Fig. 8. Consequently, digital holography measurements tend to be of

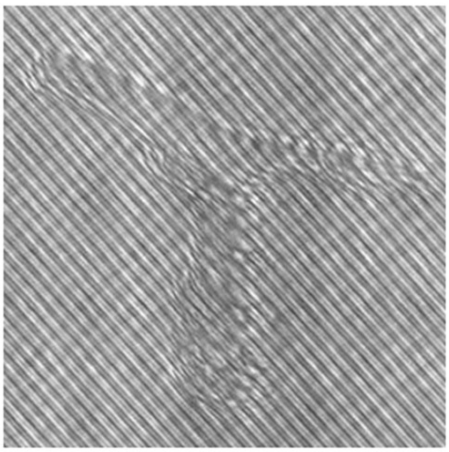

Figure 7. Off-axis fringe pattern

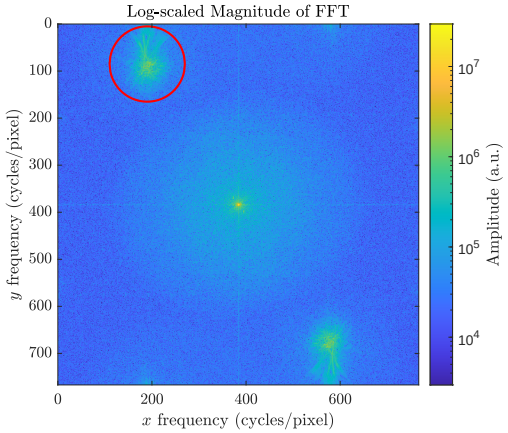


Figure 8. Fourier domain of flow induced interferogram. Signal is circled in red.

much higher resolution in comparison to Shack-Hartmann measurements and do not suffer from the limitations of beam spreading when faced with sharp density gradients.

## 3. RESULTS

To examine the thermodynamic gradients of the compressible shear layer created in our experiment, we first verified that the flow in the CSLWT corresponds to a 'canonical' shear layer. To establish this, Pitot probe measurements were taken at 0.001 m intervals to capture the velocity profile of the CSLWT. These results were then compared to the canonical shear layer described in Ref. 12. Figure 9 presents the non-dimensional experimental and canonical shear layer velocity profiles.

The x-axis of Fig. 9 represents the vertical coordinate of the Pitot probe, relative to the slip line location $y_{0.5}$, normalized by the shear-layer vorticity thickness, $\delta_w$.[6]

$$y^* = \frac{y - y_{0.5}}{\delta_w} \tag{11}$$

The shear-layer vorticity thickness is defined in Ref. 22 as:

$$\delta_w = \frac{U_2 - U_1}{\left(\frac{\partial U}{\partial y}\right)_{\max}} \tag{12}$$

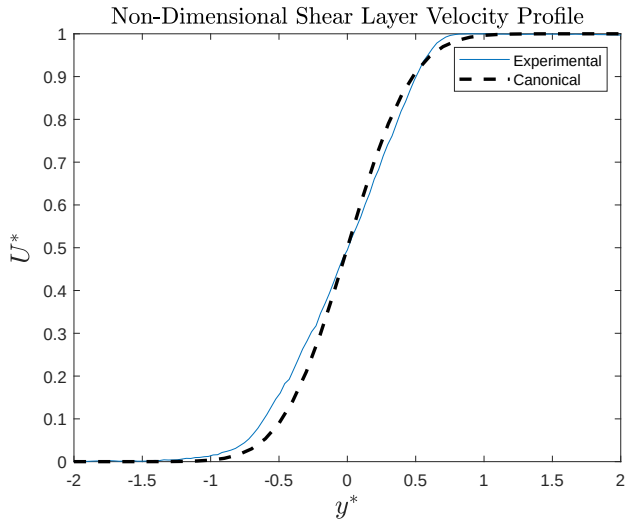


Figure 9. Non-dimensional compressible shear layer velocity profile

Here, the shear layer vorticity thickness at the measurement location was found to be $\delta_w \approx 0.0308$ m. The y-axis corresponds to the normalized velocity profile defined as:

$$U^* = \frac{U - U_1}{U_2 - U_1} \tag{13}$$

It is evident that the measured experimental velocity profile shows good agreement with the canonical shear layer described in previous studies, justifying further analysis in the context of canonical shear layer theory. To further normalize the compressible shear layer, Ref. 23 shows that spanwise uniformity can be improved by forcing the shear layer at its dominant natural convective frequency defined as the passing frequency of dominant vortical structures at the measurement location and flow speed.

To identify the dominant natural convective frequency, the ensemble averaged power spectral density (PSD) of digital holographic wavefronts was calculated for a beam passing through the unforced shear layer across multiple points located within the shear layer. This is shown in Fig. 10 where we can see a dominant natural frequency of 1230 Hz for the test conditions of $M_2$=0.71, $M_1$=0.17, and the streamwise measurement location of 0.279 m.

This frequency aligns well with Ref. 12 which characterized the dominant natural frequency of the CSLWT as a function of downstream distance shown in Fig. 11.

An example of a sequence of wavefronts for a beam passing through the forced shear layer are shown in Fig. 12 with digital holography in the top row and the corresponding SHWFS wavefronts in the bottom row. The wavefronts shown have had optical tip, tilt and piston removed in order to better examine the ability of both methods to resolve fine-scale structures within the flow. Both the Shack-Hartman and the digital-holography wavefronts show a progression of high and low OPD regions passing from left to right (in the flow direction) through the measurement beam. The low OPD regions correspond to low density (Equation (1)), and hence are caused by the low-pressure, low-density cores of the vortices in the shear layer.

The two methods show strong agreement, with a time-averaged OPD root mean square of $OPD_{RMS} = 2.17{*}10^{-7}$ m for digital holographic wavefront measurements and $OPD_{RMS} = 2.08{*}10^{-7}$ m for Shack-Hartmann wavefront measurements. $OPD_{RMS}$ is defined as:

$$\mathrm{OPD_{RMS}} = \sqrt{\frac{1}{A}\int_A \left(\mathrm{OPD}(x,y) - \overline{\mathrm{OPD}}\right)^2 \, dx\, dy} \tag{14}$$

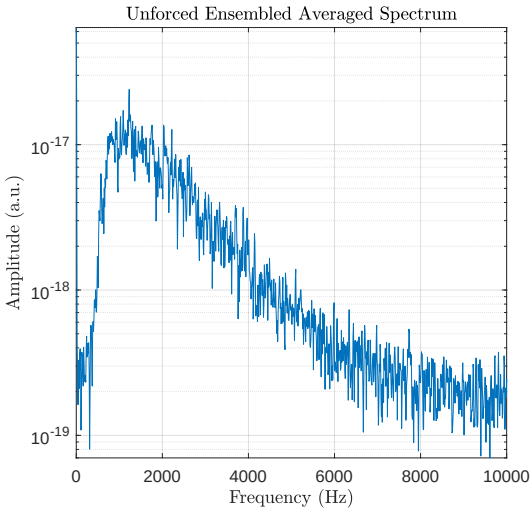


Figure 10. Unforced ensemble averaged power density spectrum averaged across a range of points within the compressible shear layer

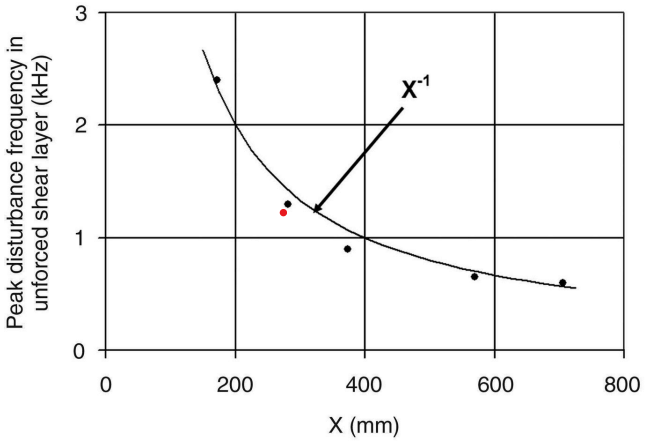


Figure 11. Dominant natural convective frequency of compressible shear layer in CSLWT as a function of downstream measurement location with our flow frequency and location shown by the red point[12]

where A is the area of the beam cross section and the overline denotes time average. The difference between the two methods is $OPD_{RMS} = 9.6 * 10^{-9}$ m or approximately 4.5%. While both methods are able to reconstruct large-scale structures in the flow with good agreement, most of the differences between the two methods are in the appearance of smaller structures.

Fig. 13a depicts a representative digital-holographic wavefront. Fig. 13b depicts the difference between Frame 1 from the digital-holographic wavefront and the Shack-Hartmann wavefront (left-most frames in Fig. 12). Here the Shack-Hartmann wavefront was interpolated to match the resolution of the digital holography wavefront. Fig. 13c shows the digital-holographic wavefront from Frame 1 with locations marked where the absolute error between the methods was greater than $2.5 * 10^{-7}$ m. As we can see, regions with large absolute error correlate with vortical structure edges within the shear layer, confirming suspicions that the Shack-Hartmann sensor is insufficiently resolving the gradients present at the edges of these features.

The Shack-Hartmann has a relatively low spatial resolution (compared to digital holography) and as a result it is unable to accurately resolve locations of sharp density and index of refraction gradients. In particular, these sharp density gradients cause variations of the index of refraction on a spatial scale smaller than the lenslet

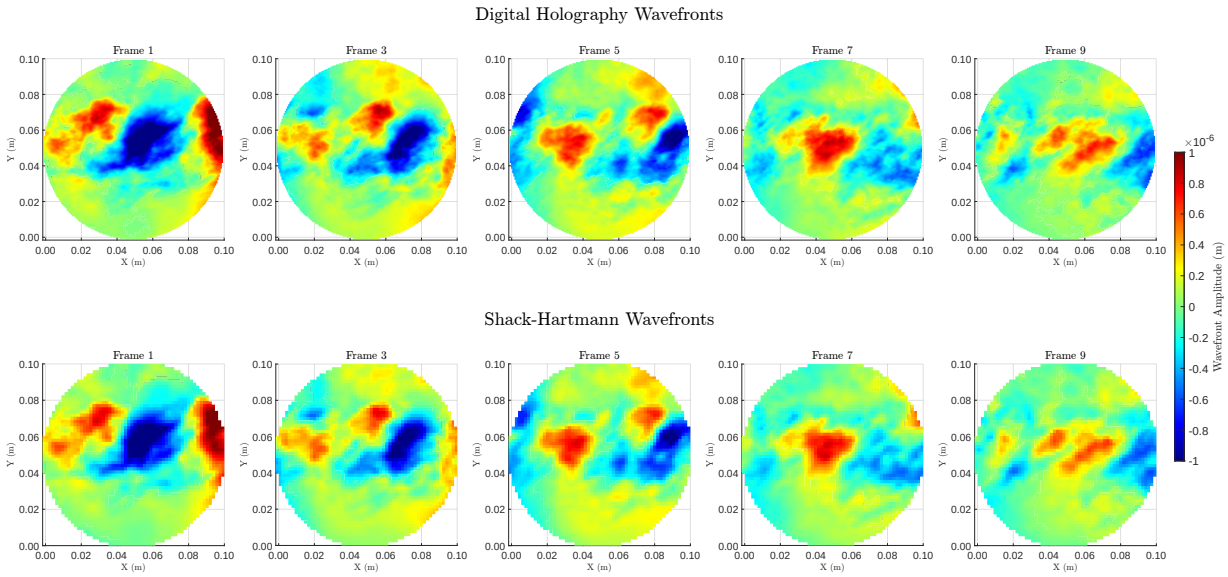


Figure 12. Digital holographic and Shack-Hartmann reconstructed wavefronts

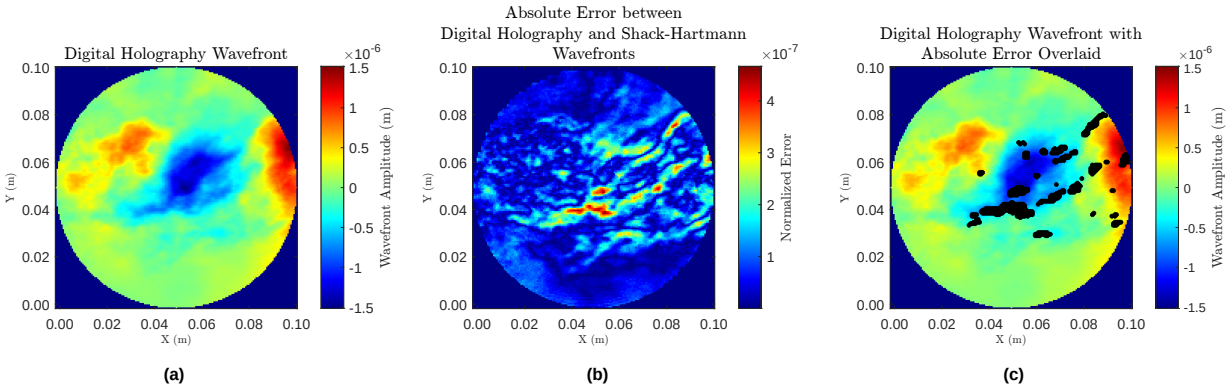


Figure 13. a) Digital holography wavefront b) Absolute error between digital holography and Shack-Hartmann wavefronts c) Digital holography wavefront with points of absolute error greater than $2.5 * 10^{-7}$ m overlaid

diameter, causing individual beamlets to spread in the farfield due to diffraction. When this occurs, the tilt calculated from the farfield irradiance centroid is no longer accurate. The result of this effect is that Shack-Hartmann wavefront measurements consistently underpredict the strength of the thermodynamic gradients in the regions with strong density gradients, as the OPD is calculated based on the centroid of each lenslet such that the calculated deflection of affected lenslets is artificially small. That is, if the light is sufficiently "smeared" by diffraction effects over the area of interest on the CCD under the lenslet, then the calculated centroid will be closer to the undeflected position than had no beam spreading occurred, and thus the calculated slope will be lower than it should be.

Moreover, the locations of appreciable beam spread as shown in Fig. 14 suggest that Shack-Hartmann is insufficiently resolving sharp gradients both at the edges of vortical structures and at the cores of these structures themselves. Fig. 14b shows a Shack-Hartmann reconstructed wavefront with locations of appreciable beam spread overlaid, where a beam-spread threshold of $\frac{D4\sigma}{D_{DL}} = 1.53$ was chosen. Here, $D_{DL}$ is the diffraction limited spot size $D_{DL} = \frac{2f\lambda}{D_{SA}}$ and $D_{SA}$ is the size of the SHWFS lenslet.[6] Here you can see many of the locations with large beam spread align with locations with large error seen in Fig. 13b. The beam spread threshold chosen for this experiment was lower in comparison to that of Ref. 6 (1.7) due to the reduced beam spreading resulting from our decreased beam size at the test section. Wells et. al. used a 0.254 m (10 inch beam) at their test section, whereas

our experiment employed a 0.1016 m (4 inch) beam. The consequence of a larger analyzing beam is that each Shack-Hartmann lenslet represents a larger area and is more likely to capture entire regions of high-magnitude phase gradients such as those along the edges of vortical structures. As a result, a single Shack-Hartmann lenslet will observe greater beam spread and D4$\sigma$ values due to the effects of higher-order aberrations.

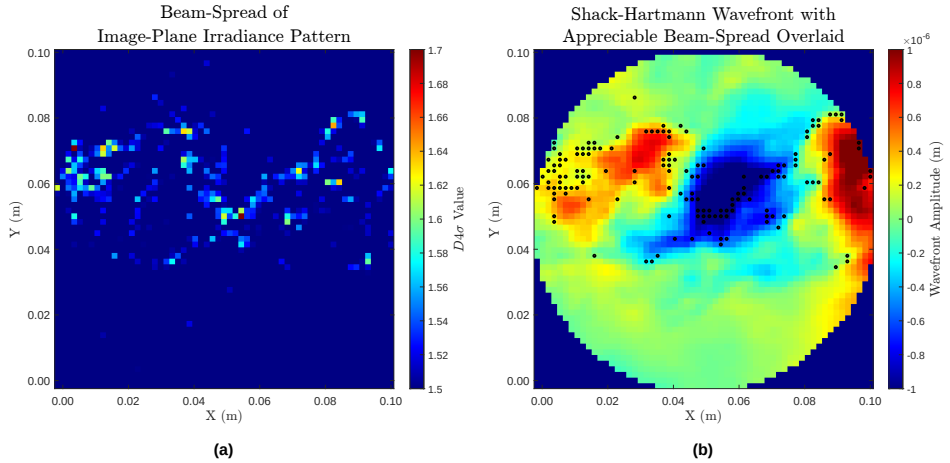


Figure 14. a) Beam-Spread values of SHWFS irradiance pattern at the image-plane b) Shack-Hartmann wavefront with locations of $D4\sigma$ greater than 1.53 overlaid

The phase gradient magnitude field of Frame 1 of Fig. 12 for both methods can be seen in Fig. 15. The figure cleary illustrates the under-predictive tendency of Shack-Hartmann wavefront measurements in regards to the magnitude of phase, and subsequently, density gradients. Here, the spatio-temporal average of Shack-Hartmann wavefronts underpredicted the magnitude of phase gradients by approximately 45% as compared to digital-holographic wavefronts. Furthermore, the ability of digital holography to capture smaller-scale content is also demonstrated.

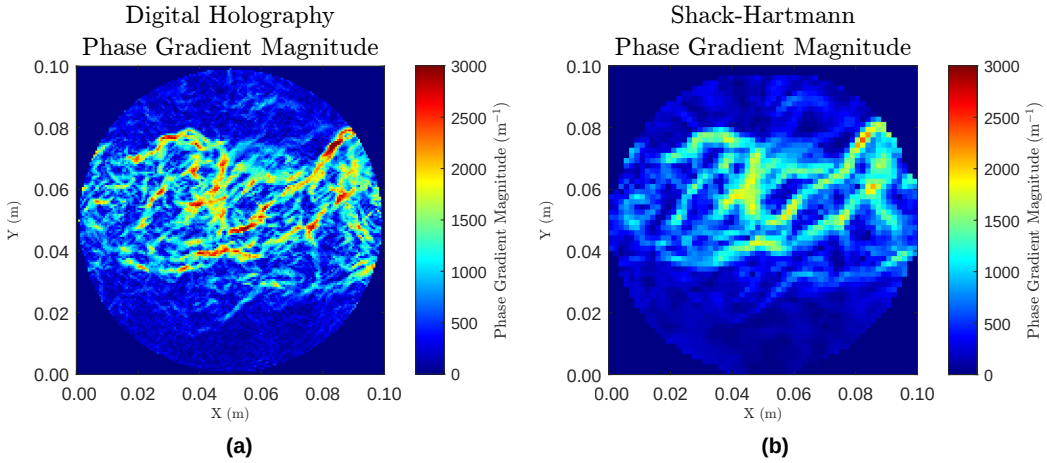


Figure 15. Phase gradient magnitude fields of digital holographic (a) and Shack-Hartmann (b) unwrapped phase maps

## 4. CONCLUSION

The experimental results show that the flow exhibits characteristics of a canonical shear layer and the applied forcing successfully regularizes the flow and improves spanwise uniformity across the test section. While both Shack-Hartman and digital-holography wavefront sensing methods yield consistent large-scale results, Shack-Hartmann systematically underestimates phase gradient magnitudes by $\sim 45\%$ in regions of the flow with large density variations. Regions exhibiting significant beam spread, large absolute error between wavefronts from both methods, and high magnitude phase gradients largely coincide, confirming suspicions that the SHWFS is insufficient for resolving high density-gradient features.

The question remains of how the high density-gradient regions observed in this experimental effort align with the thermo/fluid mechanics of the shear-layer flow. To address this, time-resolved URANS CFD computations modeling the compressible shear-layer flow examined in this paper are currently underway and reported in a companion paper, with the objective of validating the CFD performance in predicting high-magnitude thermodynamic gradients and understanding their origin.


### Acknowledgments

This work was sponsored by the Joint Directed Energy Transition Office.


## REFERENCES


[1] Tyson, R. K., "Chapter 1 - history and background," in [*Principles of Adaptive Optics*], Tyson, R. K., ed., 1–24, Academic Press (1991).

[2] Tyson, R. K., "Chapter 2 - sources of aberrations," in [*Principles of Adaptive Optics*], Tyson, R. K., ed., 25–52, Academic Press (1991).

[3] Barrell, H. and Sears, J. E., "The refraction and dispersion of air for the visible spectrum," *Philosophical Transactions of the Royal Society of London. Series A, Mathematical and Physical Sciences* **238**(786), 1–64 (1939).

[4] Gordeyev, S., Jumper, E. J., and Whiteley, M. R., [*Aero-Optical Effects: Physics, Analysis and Mitigation*], Wiley Series in Pure and Applied Optics, John Wiley & Sons, 1 ed. (2023).

[5] Bukowski, T. J., Gordeyev, S., Kalensky, M., and Kemnetz, M. R., "Study of unsteady surface flowfields on and around turrets with different protrusions," *AIAA Journal* **61**(12), 5320–5331 (2023).

[6] Wells, J., Kalensky, M., Rennie, R. M., and Jumper, E. J., "Experimental and computational investigation of laser beam propagation through a free shear layer," in [*Unconventional Imaging, Sensing, and Adaptive Optics 2023*], Dolne, J. J., Spencer, M. F., and Bose-Pillai, S. R., eds., **12693**, 1269315, International Society for Optics and Photonics, SPIE (2023).

[7] DeFoor, T., Kalensky, M., Kemnetz, M., Bukowski, T., and Spencer, M., "Shock-wave tolerant phase reconstruction algorithm for shack–hartmann wavefront sensor data," *Optical Engineering* **62** (Dec 2023).

[8] DeFoor, T. E., Bukowski, T. J., Kalensky, M., and Gordeyev, S., "Phase discontinuity classification from single-aperture irradiance patterns using machine learning," in [*Unconventional Imaging, Sensing, and Adaptive Optics 2024*], Dolne, J. J., Bose-Pillai, S. R., and Kalensky, M., eds., **13149**, 131490F, International Society for Optics and Photonics, SPIE (2024).

[9] Kalensky, M., Kemnetz, M. R., and Spencer, M. F., "Effects of shock waves on shack–hartmann wavefront sensor data," *AIAA Journal* **61**(6), 2356–2368 (2023).

[10] Kalensky, M., "Branch-point identification using second-moment shack–hartmann wavefront sensor statistics," *Appl. Opt.* **62**, G101–G111 (Aug 2023).

[11] Papamoschou, D. and Roshko, A., "The compressible turbulent shear layer: an experimental study," *Journal of Fluid Mechanics* **197**, 453–477 (Dec 1988).

[12] Rennie, M., Duffin, D., and Jumper, E., "Characterization and aero-optic correction of a forced two-dimensional weakly compressible shear layer," *Aiaa Journal - AIAA J* **46**, 2787–2795 (11 2008).

[13] Thorlabs, Inc., "Shack-hartmann wavefront sensors." https://www.thorlabs.com/newgrouppage9.cfm?objectgroup_id=5287 (2025). Accessed: 2025-05-30.

[14] Southwell, W., "Wave-front estimation from wave-front slope measurements," *J. Opt. Soc. Am.* **70**, 998–1006 (Aug 1980).

[15] Wilcox, C. C., Radosevich, C. J., Healy, K. P., Tuffli, A. L., Agena, B. D., and Mark F. Spencer, D. J. W. I., "Digital holography wavefront sensing with a super wind tunnel," **11030**, SPIE (April 2019).

[16] Spencer, M. F., "Spatial heterodyne," in [*Encyclopedia of Modern Optics (Second Edition)*], Guenther, B. D. and Steel, D. G., eds., 369–400, Elsevier, Oxford, second edition ed. (2018).

[17] Chu, E. D., Bukowski, T. J., and Gordeyev, S., "Improved wavefront reconstruction for shack–hartmann wavefront sensor in the presence of shock-related distortions," *Optics and Laser Technology* **187**, 112764 (2025).

[18] Tahara, T., Quan, X., Otani, R., Takaki, Y., and Matoba, O., "Digital holography and its multidimensional imaging applications: a review," *Microscopy* **67**, 55–67 (02 2018).

[19] Banet, M. T., Spencer, M. F., and Raynor, R. A., "Digital-holographic detection in the off-axis pupil plane recording geometry for deep-turbulence wavefront sensing," *Applied Optics* **57**, 465 (jan 2018).

[20] Banet, M. T., Spencer, M. F., Raynor, R. A., and Marker, D. K., "Digital holography wavefront sensing in the pupil-plane recording geometry for distributed-volume atmospheric aberrations," in [*SPIE Proceedings*], Dolne, J. J., Karr, T. J., and Dayton, D. C., eds., SPIE (sep 2016).

[21] Banet, M. T. and Spencer, M. F., "Multiplexed digital holography for simultaneous imaging and wavefront sensing," in [*Unconventional and Indirect Imaging, Image Reconstruction, and Wavefront Sensing 2019*], Dolne, J. J., Spencer, M. F., and Testorf, M. E., eds., **11135**, 1113503, International Society for Optics and Photonics, SPIE (2019).

[22] Rennie, M., Ponder, Z., Gordeyev, S., Nightingale, A., and Jumper, E., "Numerical investigation of two-dimensional compressible shear layer and comparison to weakly compressible model," (01 2008).

[23] Rennie, M., Siegenthaler, J., and Jumper, E., "Forcing of a two-dimensional, weakly-compressible subsonic free shear layer," *Collection of Technical Papers - 44th AIAA Aerospace Sciences Meeting* **9** (01 2006).